

Supporting Information

Rechargeable Lithium-Hydrogen Gas Batteries

Z. Liu, Y. Ma, N. Ali Khan, T. Jiang, Z. Zhu, K. Li, K. Zhang, S. Liu, Z. Xie, Y. Yuan, M. Wang, X. Zheng, J. Sun, W. Wang, Y. Meng, Y. Xu, M. Chuai, J. Yang, W. Chen**

Supporting Information for

Rechargeable Lithium-Hydrogen Gas Batteries

Zaichun Liu⁺, Yirui Ma⁺, Nawab Ali Khan, Taoli Jiang, Zhengxin Zhu, Ke Li, Kai Zhang, Shuang Liu, Zehui Xie, Yuan Yuan, Mingming Wang, Xinhua Zheng, Jifei Sun, Weiping Wang, Yahan Meng, Yan Xu, Mingyan Chuai, Jinlong Yang⁺, Wei Chen⁺

This file includes:

- Experimental section
- Calculation details
- Figures S1 to S18
- Tables S1 to S4
- References

Experimental Section

Preparation of Pt/C cathode. The Pt/C cathode was prepared by mixing commercial Pt/C powder and a PVDF binder with a mass ratio of 9:1 in NMP solvent and stirred vigorously overnight. The above slurry was then cast onto one side of the GDL and completely dried at 60 °C for 12 hours in a vacuum oven. The mass loading of Pt/C was controlled to be 0.1 mg cm⁻². The Ru/C cathode was fabricated by the same method except that the commercial Ru/C powder was used instead of Pt/C.

Preparation of Li_{1.3}Al_{0.3}Ti_{1.7}(PO₄)₃ (LATP) solid electrolyte. Typically, the LATP powder (0.4 g) was pressed under a pressure of 25 tons for 2 min to form a disc with a diameter of 12.7 mm or 18.0 mm at room temperature. The resulting white disc was sintered at 850 °C for 10 hours, with a programmed heating rate of 10 °C min⁻¹ and natural cooling.

Preparation of Li₃PO₄ filled Li_{1.3}Al_{0.3}Ti_{1.7}(PO₄)₃ (LATP) solid electrolyte. Typically, the Li₃PO₄ powder (0.5 g) was dissolved into 20 mL DMSO solution and continuously stirred to form suspension. We took 10-15 μL of this suspension and dropped it evenly onto the single side of the prepared LATP pellet. The resulting processed LATP pellet was sintered at 850 °C for 2 hours, with a programmed heating rate of 10 °C min⁻¹ and natural cooling.

Preparation of recrystallized LiH₂PO₄ or mixed LiOH and LiH₂PO₄ solid electrolyte. Typically, different amounts of LiH₂PO₄ or mixed LiOH and LiH₂PO₄ aqueous solution were dropped into GF/8 or GF/B, and then vacuum dried in an oven at 80 °C for 12 hours. During the test, 10~20 μL H₃PO₄ was added to wet the interface between the electrolyte and cathode catalyst.

Preparation of PAM-hydrogel electrolyte. The hydrogel electrolyte was prepared by dissolving 5.8 g AM in 20 mL solution, followed by the addition of 28.5 mg APS and 3.5 mg MBAA. The solution was placed under rigorous stirring until the solids were completely dissolved. Afterwards, the solution was injected into rubber molds (thickness of 1 mm) and covered with a glass plate. The sample was kept at 80 °C for 12 hours to allow for complete polymerization to form a gel. The gel was immersed in the electrolyte (1 M LiTFSI in 12 M H₃PO₄) for 2 hours, then dried at 80 °C for 3 hours.

Fabrication of Swagelok cells. The Swagelok cell was composed of stainless-steel inlet and outlet valves with Klein Flange (KF) to Swagelok adapters in a polytetrafluoroethylene (PTFE)-centered O-ring by a clamp, as illustrated in Figure S1, which was well developed in our previous studies.^[1] Typically, the anode part was assembled in an Ar-filled glove box (Vigor, O₂ < 0.1 ppm and H₂O < 0.1 ppm) by stacking a lithium foil (thickness of 450 μm), the LATP solid electrolyte in a 2025-type coin cell with one-sided hole (area of 0.2 cm² or 1.0 cm²). The above anode was transferred outside of the glove box and then sandwiched with the Pt/C cathode by a proton-rich electrolyte-filled GF/B and assembled in a typical coin-cell stack into the Swagelok cell, in which the proton-rich electrolyte-filled GF/B was in direct contact with the LATP solid electrolyte through the provided hole in the 2025-type coin cell. Both sides of the 2025-type coin cell were protected with corrosion-resistant adhesive tape and Parafilm, and a high-purity Ti mesh were used as conductive current collectors for the cathode, to avoid any possible contamination or side reactions. In the cathode, the Pt/C-coated side was in a direct contact with the proton-rich electrolyte-filled GF/B and the other side was employed as a gas diffusion layer. The electrolyte on the anode side

was 15 μL of 1.0 M LiPF_6 based organic liquid electrolyte while the proton-rich electrolyte on the cathode side was 25 μL of 1 M LiTFSI in 12 M H_3PO_4 . The proton-rich electrolyte on the cathode side for its utilization testing was 25 μL of 0.1 M LiH_2PO_4 in 10 M, 12 M or 14.5 M H_3PO_4 solutions with GF/8. An insulating PTFE film was placed on the outer surface of the anode side of the stainless steel KF adapter to electrically insulate the cathode and anode by sealing with the clamp. High-purity hydrogen gas (99.99%, Airgas) was filled into the assembled cell to remove the trapped air. The valves were then locked, and the Swagelok cell was tested under the sealed condition. In the anode-free Li-H cell, a pristine Li-free Cu foil current collector was used as the anode and a single layer of $\text{sAl}_2\text{O}_3/\text{PE}$ soaked with a tiny amount (15 μL) of $\text{LiTFSI}/\text{DOL-DME}$ based organic electrolyte was sandwiched between the LAMP and Cu foil. The electrolytes on the cathode of anode-free Li-H cells were the recrystallized LiH_2PO_4 or mixed LiH_2PO_4 and LiOH solid electrolytes with an effective reaction area of 1.0 cm^2 . Other structures and compositions of the anode-free cells were fabricated in the same manner as that of the Li-H cells.

Electrochemical measurements. All galvanostatic charge-discharge and open-circuit voltages measurements of the cells were tested on a VMP3 electrochemical workstation (Biologic, France) and battery testing systems (LandHe and Neware). In the galvanostatic charge-discharge measurements, a technique of constant current with cut-off capacity was adopted to the charge process and a constant current with cut-off potential was applied to the discharge process of the cells. During the long-term cycling test in Figure 3b, we supplemented the cell with H_2 after the operation for 1000 hours. During the testing process of H_2 utilization, we assembled and sealed the Li-H Swagelok cells in a nearly atmospheric pressure Ar glove box, and then transferred the cells out of the glove box for relevant testing. The electrochemical impedance spectra with a frequency range of 1 MHz to 100 mHz were collected using a Biologic VMP3 multi-channel electrochemical workstation. Gas chromatography measurements were performed on a GC-2014C gas chromatograph (SHIMADZU) with Ar as the carrier gas. The refrigerator used to carry on the low temperature test was set at a constant temperature of $-20\text{ }^\circ\text{C}$, and the machine has an intrinsic temperature fluctuation of $\pm 2\text{ }^\circ\text{C}$ which results from the intermittent operation of compressor.

Characterizations. Scanning electron microscope (SEM, JEOL-6700F) was carried out to characterize the morphologies, sizes and structures of the Pt/C powder and LAMP solid electrolyte. Powder X-ray diffraction (XRD) patterns were collected on a Philips X'Pert PRO SUPER X-ray diffractometer equipped with graphite monochromatized $\text{Cu K}\alpha$ radiation. X-ray photoelectron spectroscopy (XPS, Thermo ESCALAB 250Xi) was performed with Al $\text{K}\alpha$ source. To conduct SEM imaging and XRD test on the interface between LAMP solid electrolyte and GF supported proton-rich electrolyte in the actual battery, the battery was firstly opened in air and the anode coin cell part was immediately transferred to the glove box. The LAMP solid electrolyte was taken out and washed with absolute alcohol to remove any electrolytes on both sides. The washed LAMP solid electrolyte was dried in a vacuum oven at $80\text{ }^\circ\text{C}$ overnight and sealed for characterization. To conduct SEM imaging and XPS test on the solid electrolyte interphase (SEI) on the surface of Li-metal after cycling in the actual battery, the anode of the battery was firstly opened in an argon filled glove box. The Li metal anode was then taken out of the opened battery and washed with DMC to remove any electrolytes.

The clean and naturally dried anode was sealed and quickly transferred to SEM or XPS instrument to avoid any water and oxygen exposure. The SEI on the Cu surface of the anode-free Li-H cells were also characterized by the same operational steps as that of the Li metal-H cells. All the cross-sectional samples were polished by ion beam polisher before the SEM observation to show a clear and authentic Li deposition morphology. Differential scanning calorimetry (DSC) was carried out in DSC Q2000 by scanning from -90 °C to room temperature at a rate of 5 °C min⁻¹.

DEMS test. A typical Li-H battery was assembled without pre-loading of H₂. The Swagelok cell was connected to a DEMS (LingLu Instruments, Shanghai, China) by two tubes as the gas inlet and outlet. High purity Ar gas was used as the carrier gas and purifying gas. Before the electrochemical reaction, the sealed electrolytic cell was purified with Ar gas at 1.2 mL min⁻¹ for 20 min to eliminate the air inside the device. Afterwards, the Li-H battery was set at the discharge stage (hydrogen evolution reaction at the cathode) under a current density of 1.0 mA cm⁻². Meanwhile, the carrier Ar gas flow was maintained at 2.4 mL min⁻¹ to facilitate the H₂ detection. The y axis of Figure S2d was transformed from the original unit F (ppm) to gas generation speed v (nmol min⁻¹) by the equation: $10^9 \times F \times v_{carr} \times 4.46 \times 10^{-5} = v$, where v_{carr} represent the flow of carrier Ar gas and 4.46×10^{-5} is the transition parameter.

Solid-state NMR test. Nuclear magnetic resonance (NMR) (Bruker AVANCE III 400 WB, 20 °C) was utilized for the solid-state NMR test. Several Li-H batteries with pure LATP were assembled using typical proton-rich electrolyte and were cycled under the current density of 0.5 mA cm⁻². The as-cycled batteries were then disassembled and the LATP pellets were carefully cleaned using both DI water and ethanol for 3 times. Two types of the LATP powder were further collected after baking. Type 1 was collected by scratching the as-prepared LATP pellets surface that faced the proton-rich electrolyte which is denoted as surface. And type 2 was the rest of the LATP pellets which is denoted as bulk.

Calculations of energy densities and energy cost

The theoretical energy density is calculated based on the one-electron-transfer Li⁺/Li and H⁺/H₂ reaction, which is up to 2825 Wh kg⁻¹ with respect to the mass of discharge products of solid lithium salts and H₂ as summarized in table S1. The achieved energy density in the anode-free Li-H battery is ~ 177 Wh kg⁻¹ based on the weight of the components including active materials and their utilization of cathode catalyst (m_{PVC} or $m_{Ru/C} = 0.0001$ g), GDL ($m_{GDL} = 0.0251$ g), H₂ (125 %, $m_{H_2} = 0.0018653$ g), lithium salt (75%, $m_{LiH_2PO_4} = 0.058158$ g and 50%, $m_{LiOH} = 0.008934$ g), Cu foil ($m_{Cu} = 0.00358$ g), organic electrolyte ($m_{oe} = 0.0000059$ g), sAl₂O₃/PE film ($m_p = 0.003$ g), GF ($m_{gf} = 0.0157$ g), LATP solid electrolyte ($m_{LATP} = 0.15727$ g) and excessive 10% H₃PO₄ for wetting ($m_{H_3PO_4} = 0.007311$ g), but not considering the casting materials (i.e., stainless-steel cell case, Ti mesh) as the usual estimation at the lab level. The weight of pressure vessel of H₂ gas storage tank is expected to be controlled at 11% of the total weight after cell design engineering referring to the traditional Ni-H₂ battery. [2] The weight of solid electrolyte and organic electrolyte are calculated from the reaction effective area, which is the hole size in anode cell casing (1.0 cm²) as shown in Figure S17a. Similarly, the achieved energy cost of the battery is dependent on the above materials. The values of capacity and voltage for the calculation of energy densities are 20 mAh and 2.8 V, respectively. More calculation details can be found in table S3.

Simulation details. All calculations were performed with the standard DFT as implemented in Vienna ab initio Simulation Package (5.4.4 VASP) within the generalized gradient approximation (GGA) as formulated by the Perdew–Burke–Ernzerhof (PBE) functional. ^[3] An energy cutoff of 520 eV was applied, and Brillouin zone was sampled with a $3 \times 3 \times 1$ k-points using the Monkhorst-Pack scheme grid for geometry optimization and self-consistent calculations. All atomic positions were fully relaxed until the forces on each atom became smaller than $0.02 \text{ eV } \text{\AA}^{-1}$, and the convergence criteria for energy were set to be 10^{-5} eV . A simulation cell of $\text{Li}_8\text{Al}_2\text{Ti}_{10}\text{P}_{18}\text{O}_{72}$ was established for LATP using a supercell with six units as shown in Figure S14a. The minimum energy paths (MEPs) of Li jumps between the neighboring M1 sites and H jumps between the neighboring oxygen sites were obtained by means of the nudged elastic band (NEB) method. ^[4] The threshold for the total force that is acting on the NEB images of the interpolated reaction path was set to $0.02 \text{ eV } \text{\AA}^{-1}$. For the color-filled charge density difference of Figure 4c, yellow and cyan colors represent charge accumulation and charge depletion zones, respectively (the isosurface value is $0.002 \text{ eV } \text{\AA}^{-3}$). As shown in Figure S14b, one lithium vacancy was provided for the calculation of Li migration, while two for H migration next to TiO_6 octahedra, PO_4 tetrahedra and three for H migration next to AlO_6 octahedra. A simulation cell of LATP (002) surface with the 14.5 M H_3PO_4 cathode electrolyte model contains $\text{Li}_{16}\text{O}_{144}\text{Al}_4\text{P}_{36}\text{Ti}_{20}$, 30 H_3PO_4 and 28 H_2O molecules were established for the interface between high concentration H_3PO_4 electrolyte (14.5 M) and LATP. A simulation cell of LATP (002) surface with the water-based cathode electrolyte model contains $\text{Li}_{16}\text{O}_{144}\text{Al}_4\text{P}_{36}\text{Ti}_{20}$ and 60 H_2O molecules were established for the interface between water and LATP. Ab initio molecular dynamics simulations were carried out with the canonical ensemble (NVT) at 300 K, with a total duration of 10.0 ps and a step length of 1.0 fs. Some of the data were processed by the VASPKIT Besides. ^[5] The DFT-D3 method was used to account for van der Waals correction. The simulation time was long enough to ensure reaching the equilibrium states of the electrolyte systems. Bond-valence (BV) calculations were performed using the 3DBVSMapper package. The interaction region indicator (IRI) analysis were processed by the Multiwfn. ^[6]

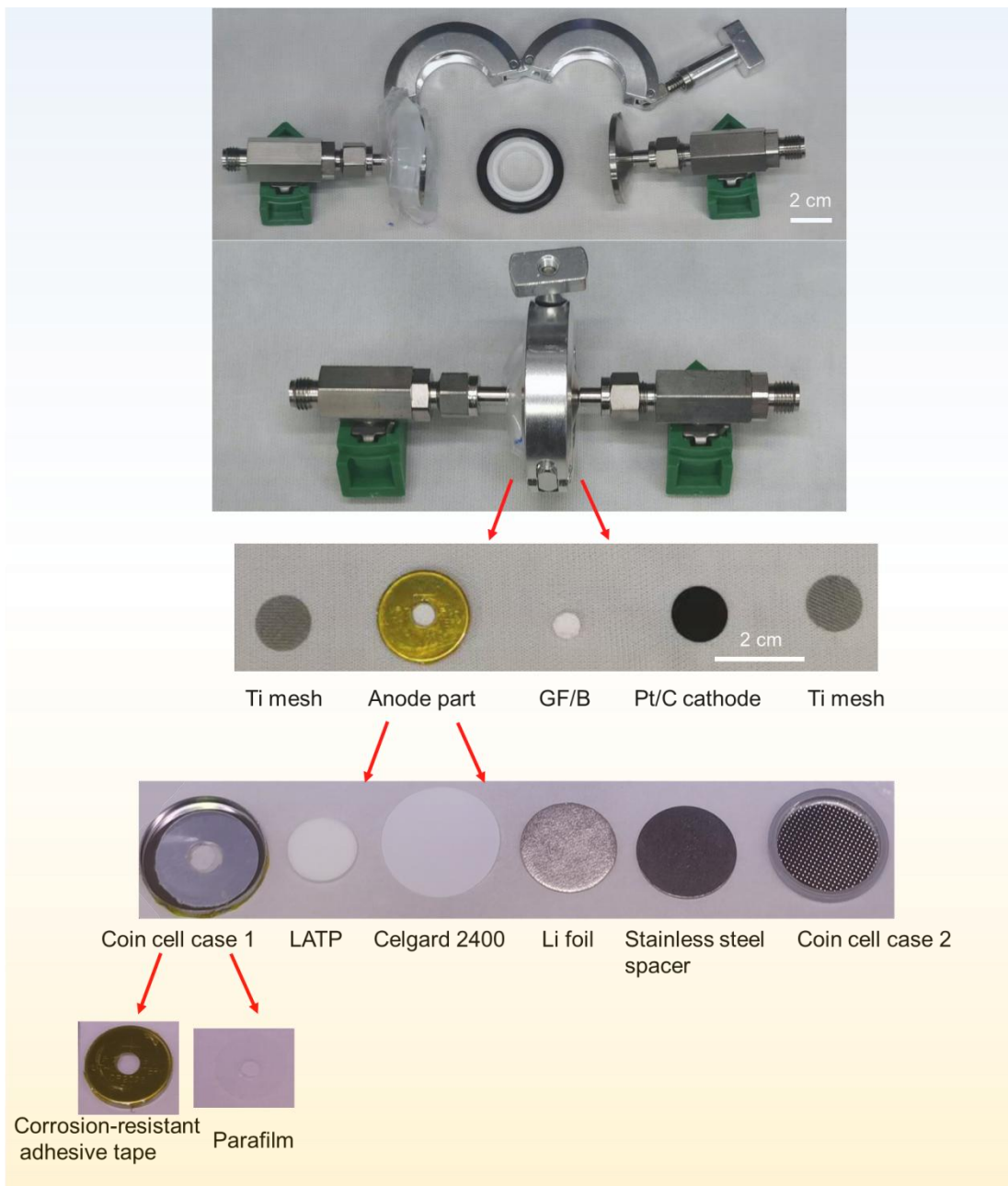


Figure S1. The setup of the Swagelok-type Li-H cell.

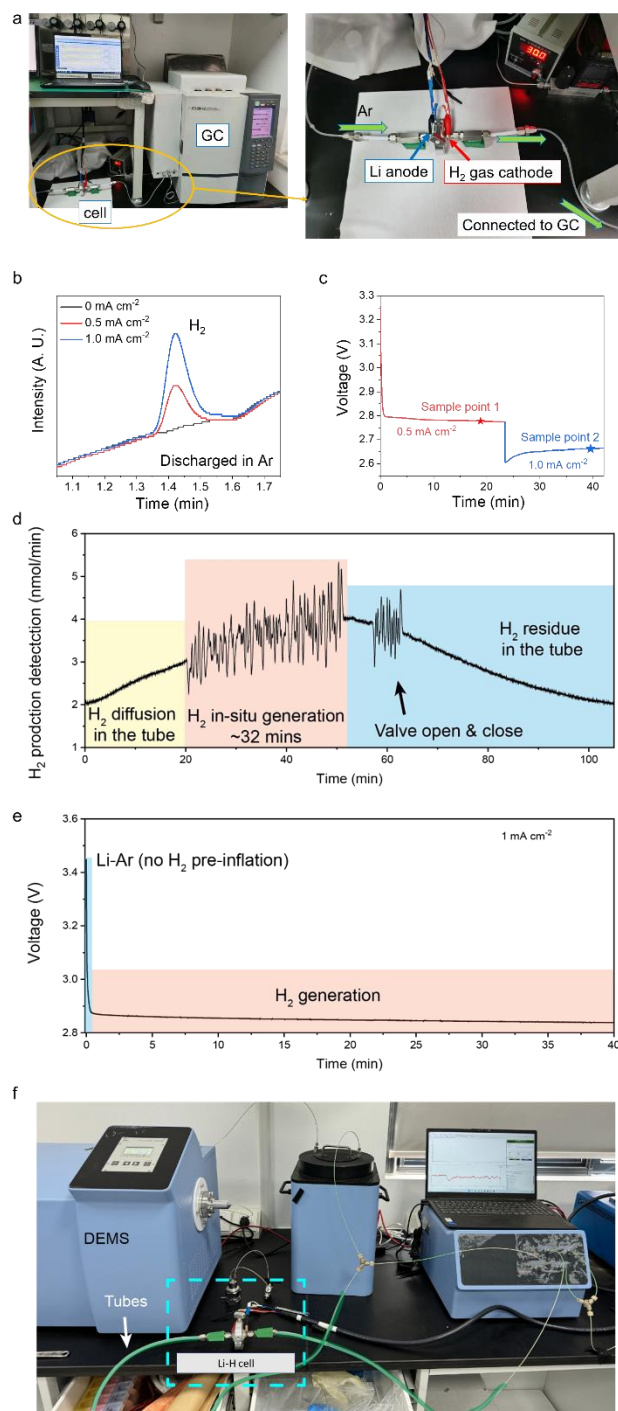


Figure S2. The GC and DEMS analysis of the Li-H cell. (a) The GC analysis setup of the Li-H cell. Variation of H₂ production of Li-H cell with 12.5 M H₃PO₄ cathode electrolyte under different discharge current densities (b), and the corresponding discharge curve (c). DEMS analysis of H₂ evolution in Swagelok Li-H cell with 14.5 M H₃PO₄ cathode electrolyte (d). The corresponding voltage profile of the Swagelok Li-H battery (e). Experimental setup of DEMS system where the gas pathway of the battery was highlighted in green (f).

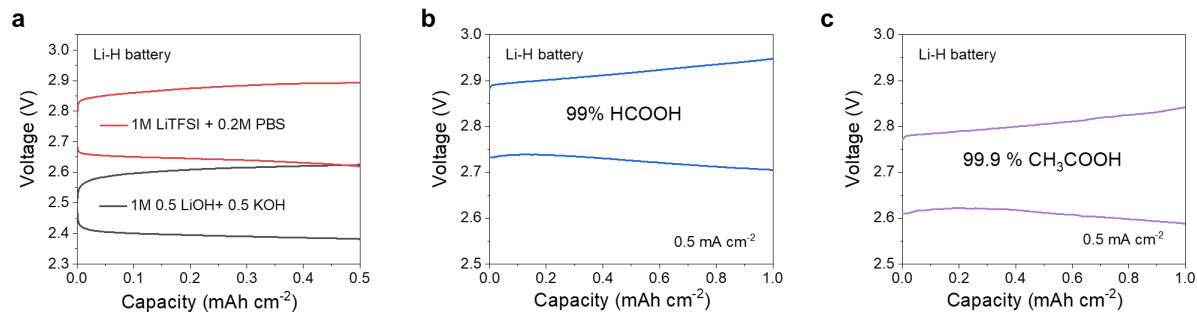


Figure S3. The universality of H₂ gas cathode battery chemistry. (a) Galvanostatic voltage profiles of the Li-H cells with neutral and alkaline cathode electrolytes. Galvanostatic voltage profiles of the Li-H cells with other typical acidic cathode electrolytes of **(b)** formic acid (HCOOH) and **(c)** acetic acid (CH₃COOH).

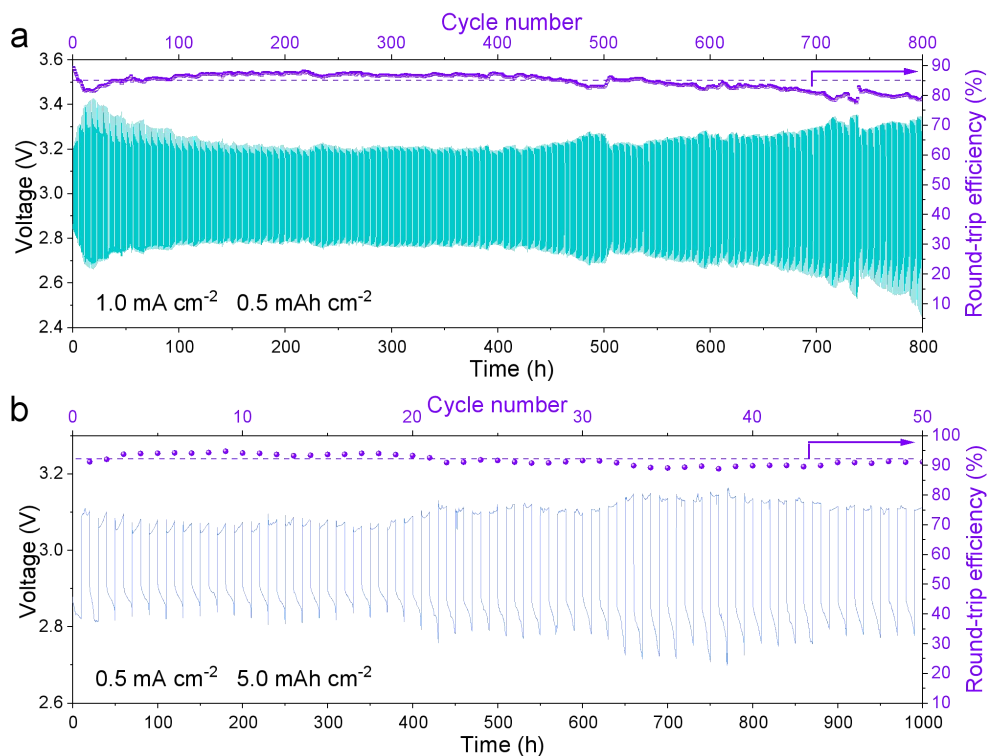


Figure S4. Cycling performance of Li-H cell at a current density of 1.0 mA cm^{-2} with a fixed capacity of 0.5 mAh cm^{-2} (a) and at a current density of 0.5 mA cm^{-2} with a fixed capacity of 5.0 mAh cm^{-2} (b).

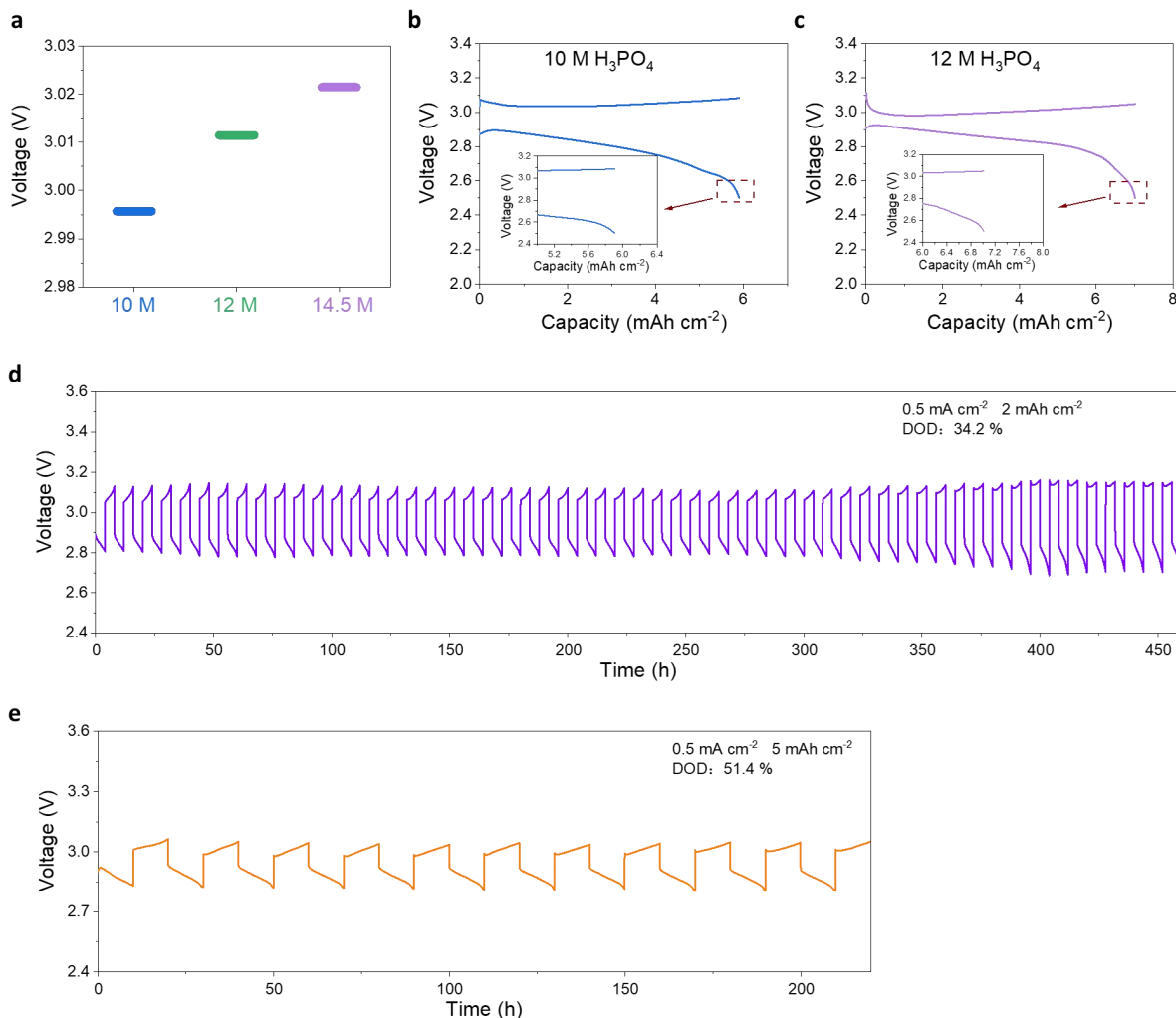


Figure S5. Performance of Li-H battery with different concentrations of H_3PO_4 electrolytes and different depths of discharge (DOD). (a) OCV of the Li-H battery with different concentrations of H_3PO_4 electrolytes. Discharge/charge curves at fully discharged and charged states of the Li-H cell with (b) 10 M and (c) 12 M cathode H_3PO_4 electrolytes at a current density of 0.5 mA cm^{-2} . (d) Cycling performance of Li-H cell at a set capacity of 2 mAh cm^{-2} with a $15 \mu\text{L}$ 14.5 M H_3PO_4 cathode electrolyte. (e) Cycling performance of Li-H cell at a set capacity of 5 mAh cm^{-2} with a $25 \mu\text{L}$ 14.5 M H_3PO_4 cathode electrolyte.

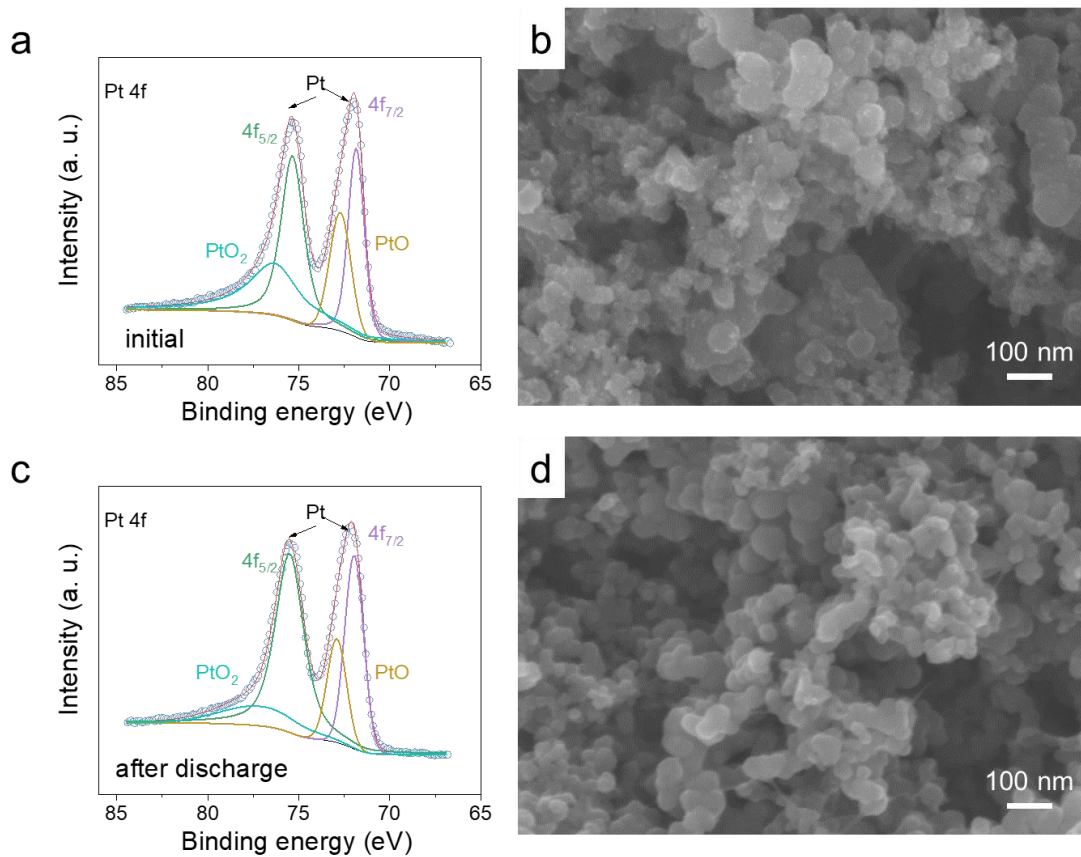


Figure S6. Characteristics of the Pt/C cathodes. (a), (c), XPS and (b), (d), SEM images of the Pt/C cathode before (a, b) and after 50 cycles (c, d) in the Li-H cell.

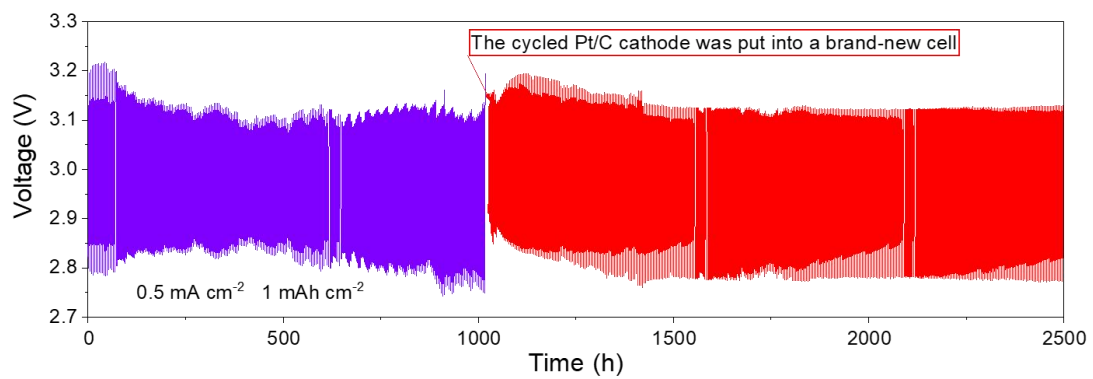


Figure S7. Recycling of the Pt/C catalyst for the Li-H battery.

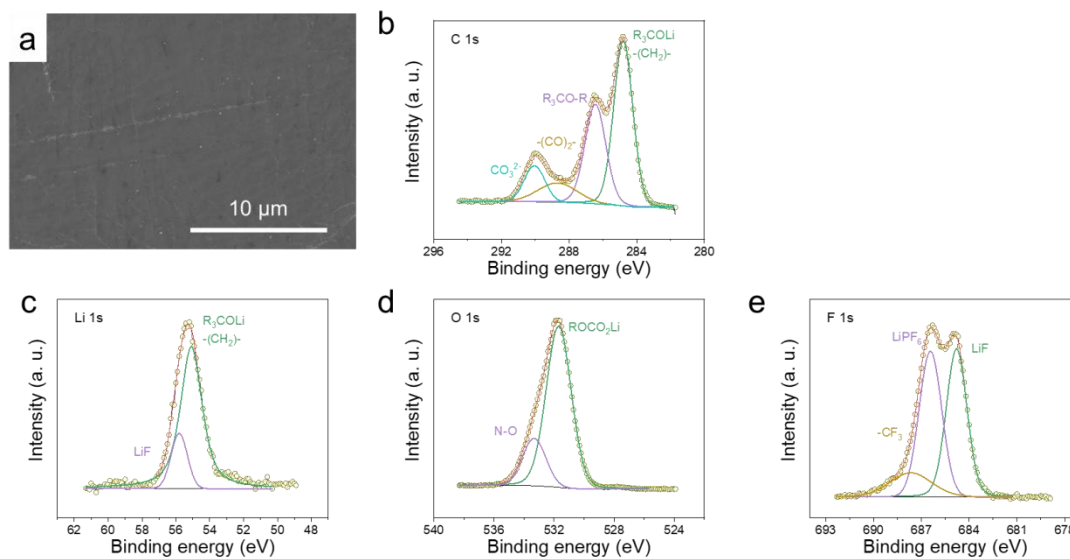


Figure S8. Characteristics of the SEI on Li metal anode surface after 50 cycles. (a) Surface morphology and the corresponding high resolution XPS spectra of carbon (C 1s) (b), lithium (Li 1s) (c), oxygen (O 1s) (d), and fluorine (F 1s) (e).

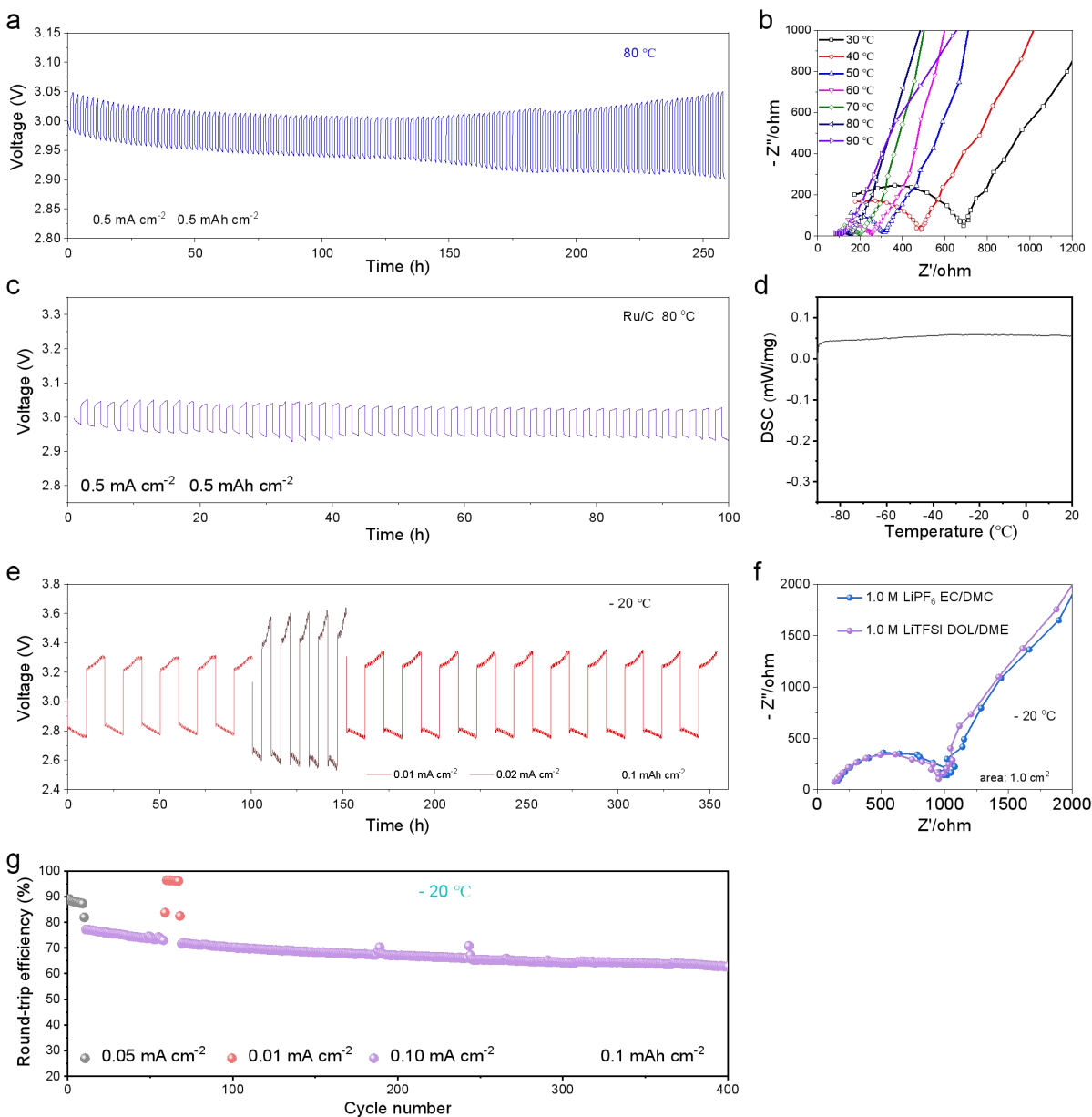


Figure S9. Characteristics of Li-H cells at all-climate conditions. (a) Long-term cycling performance of the Li-H cells at 80 °C. It was noticed that the polarization of the battery continues to increase over cycling. This is related to the volatilization of organic carbonate electrolyte wetting the solid-solid interface under long-term and high temperature cycling. (b) Impedance measurements of the composite electrolyte from 30 °C to 90 °C (area: 0.2 cm²). (c) Long-term cycling performance of the Li-H cells with Ru/C cathode catalyst at 80 °C. (d) DSC of the proton-rich-electrolyte from -90 to 20 °C. (e) Long-term cycling performance of the Li-H cells with proton-rich-electrolyte-based cathode supported with GF/B at -20 °C. (f) Impedance measurements of the composite electrolyte at -20 °C (area: 1.0 cm²). (g) RTE of the Li-H cells with the PAM hydrogel-based cathode electrolyte at -20 °C, which is corresponding to the Figure 3i.

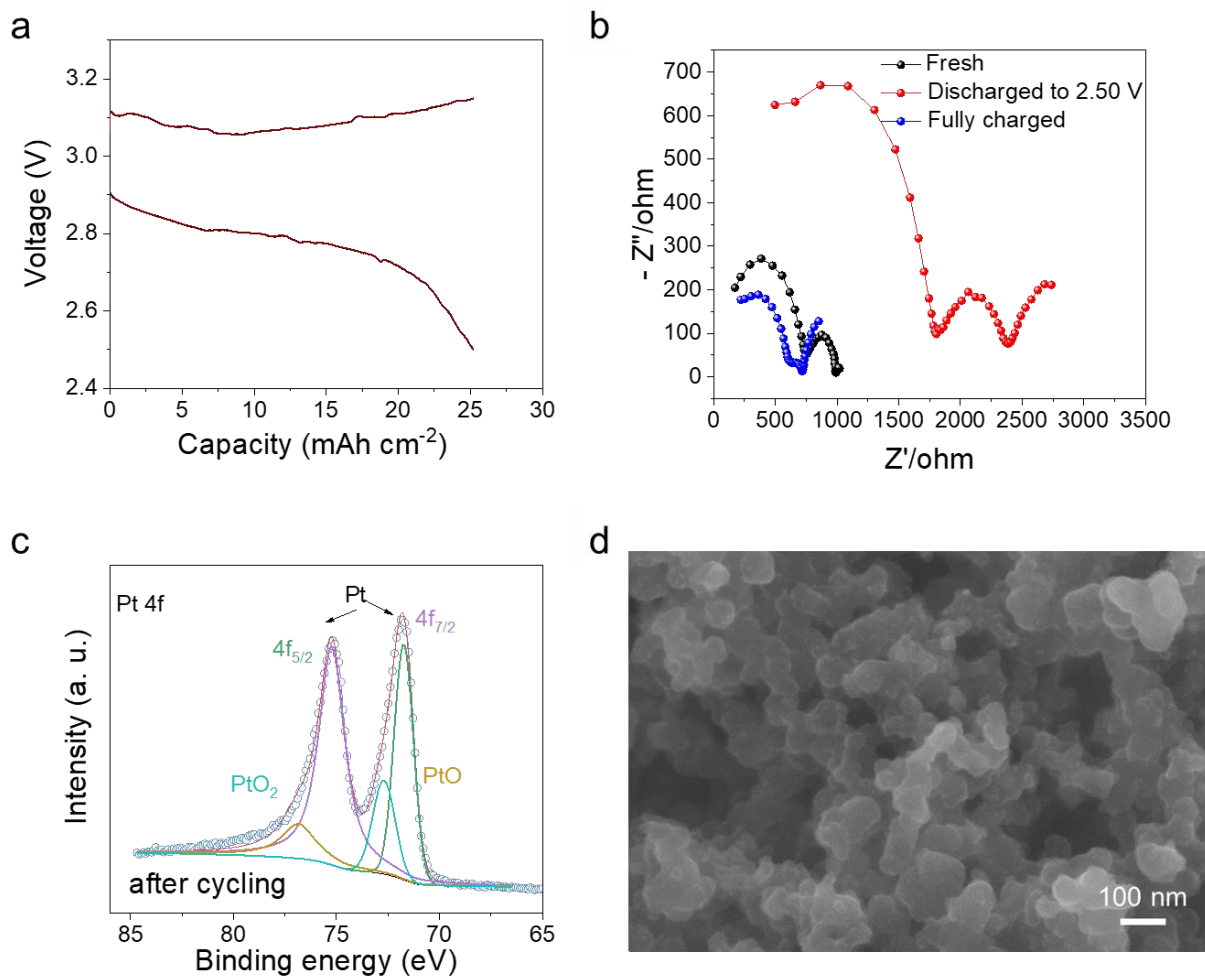


Figure S10. A high-capacity Li-H battery. Discharge/charge curves (a) and the corresponding impedance measurements (b) at the fully discharged and charged states in the first cycle of the Li-H cell at a current density of 0.5 mA cm^{-2} . XPS (c) and SEM image (d) of the Pt/C cathode after fully discharged to 2.5 V in the Li-H cell.

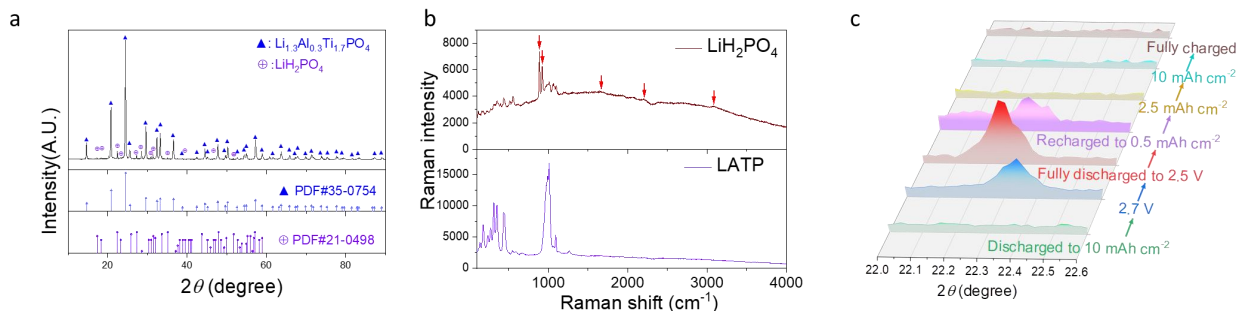


Figure S11. Characteristic of LiH_2PO_4 in the interface between LATP solid electrolyte and GF supported proton-rich electrolyte in Li-H cells. XRD patterns (a) and Raman (b) analysis after Li-H cells were fully discharged. The XRD characteristic peaks of LiH_2PO_4 (purple, PDF#21-0498) were detected at the interface. The red arrows in the Figure S11b indicate Raman characteristic peaks of LiH_2PO_4 that are different from the fresh LATP, in which the peaks at $892/928\text{ cm}^{-1}$ correspond to PO_4 and these above 1100 cm^{-1} with weak intensities correspond to OH vibrations. (c) Ex-situ XRD patterns of LiH_2PO_4 (111) on the LATP solid electrolyte surface of the Li-H cells in different discharge/charge states. LiH_2PO_4 was generated when the Li-H cell was discharged to a certain extent and can be reduced during charging.

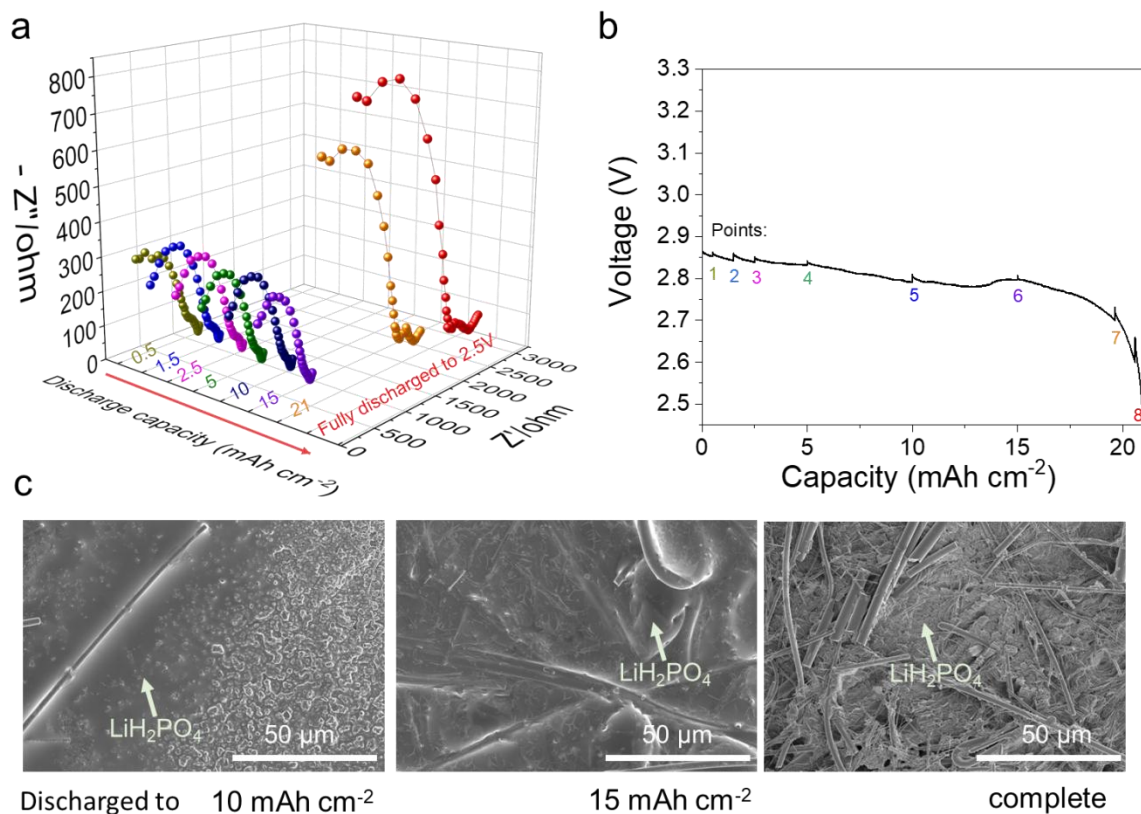


Figure S12. EIS and SEM images of the interface between LATP solid electrolyte and GF supported proton-rich electrolyte at different discharge stages. EIS (a) at eight points along the discharge curve (b) of the Li-H cell. (c) SEM images of the surface of LATP solid electrolyte at different battery discharge stages.

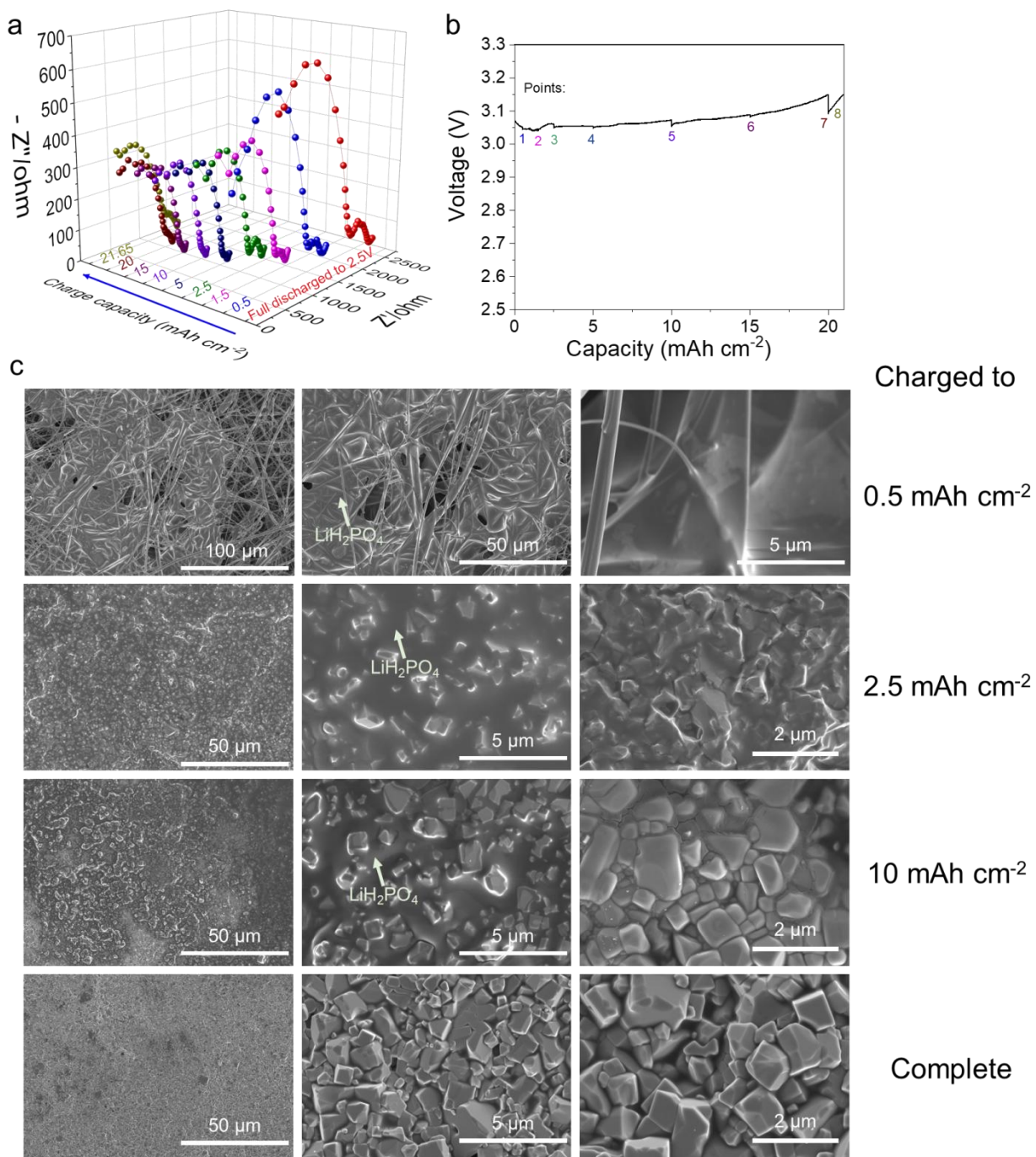


Figure S13. EIS and SEM images of the interface between LATP solid electrolyte and GF supported proton-rich electrolyte at different charge stages. Impedance measurements (a) at eight points along the charge curve (b) of the Li-H cell. (c) SEM images of the surface of LATP solid electrolyte at different battery charge stages.

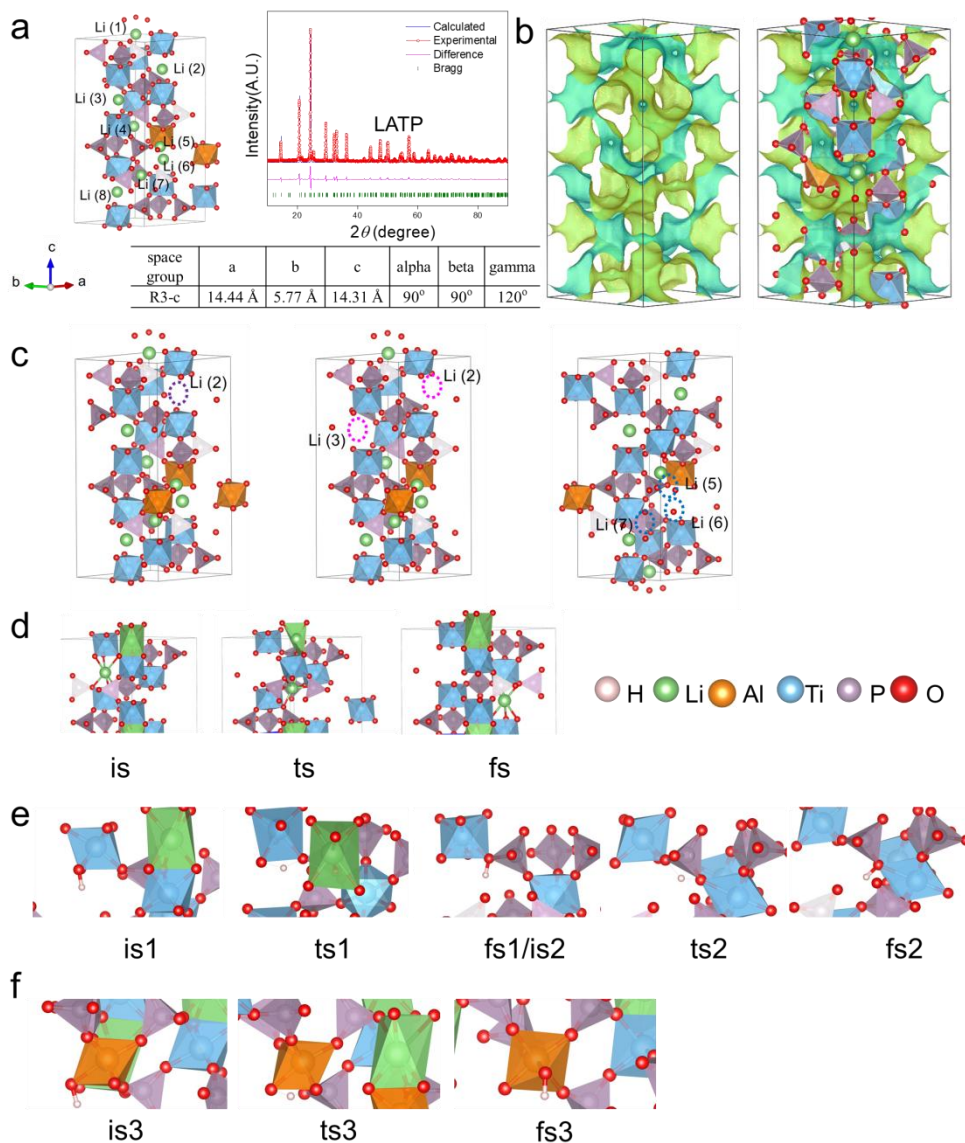


Figure S14. DFT calculation structures and their corresponding ion migration paths. (a) Structure and unit cell parameters as well as Rietveld refinement of experimental and calculated XRD patterns of LATP compound used in the DFT calculations. (b) BV calculations for the visualizable ion transfer channels in LATP. (c) One Li vacancy was provided for the calculation of Li migration, while two for H migration near TiO_6 octahedra and PO_4 tetrahedra, and three for H migration near AlO_6 octahedra. (d) Structures of the initial state (is), transition state (ts) and final state (fs) for the migration step of Li jumps between the neighboring M1 sites in LATP. Structures of is, ts and fs for the migration step of H jumps between the neighboring oxygen in LATP near TiO_6 octahedra, PO_4 tetrahedra (e) and AlO_6 octahedra (f).

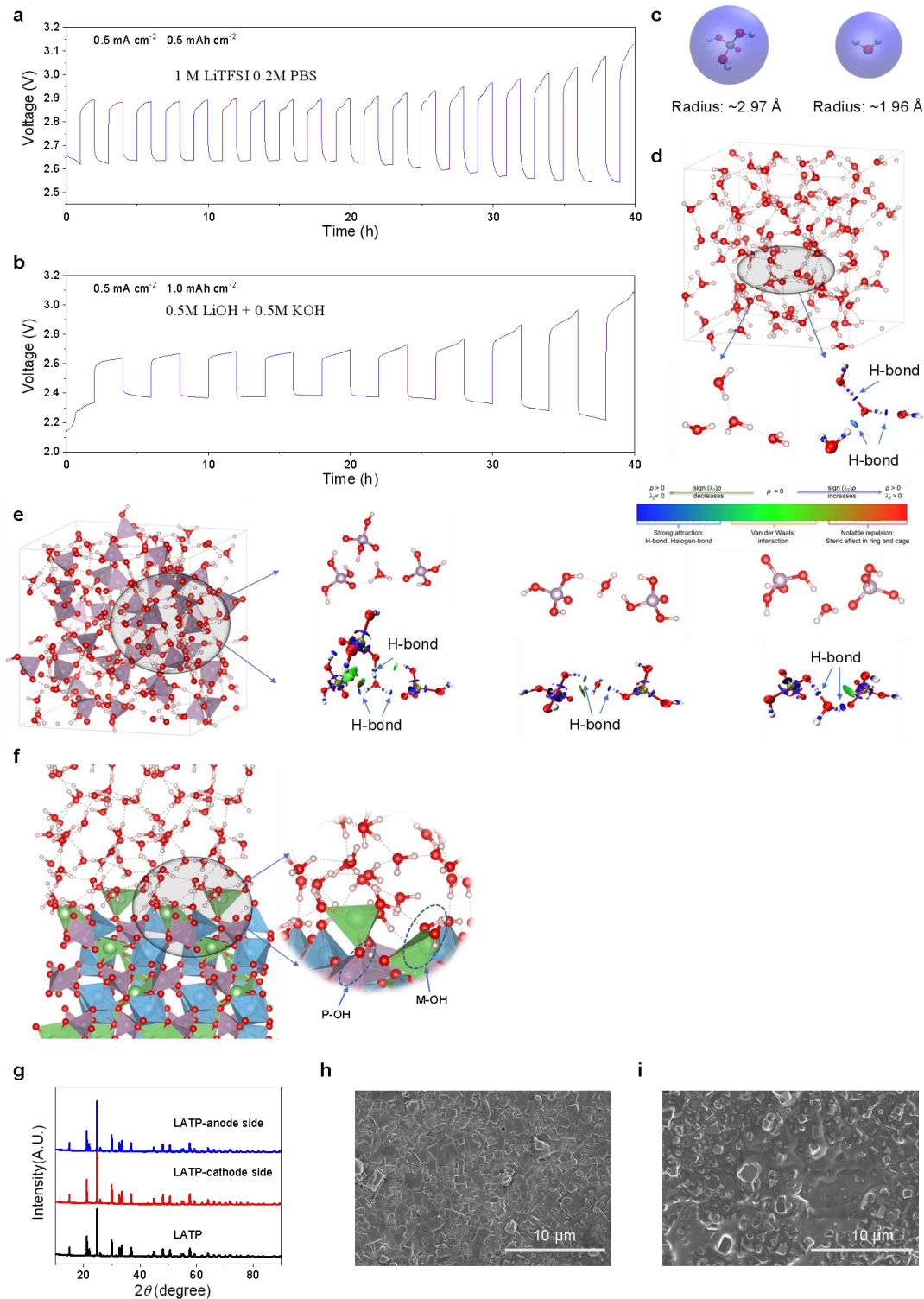


Figure S15. Stability of LAMP in H₃PO₄ electrolyte. (a) Cycling stability of Li-H battery with neutral electrolyte at a current density of 0.5 mA cm⁻² with a fixed capacity of 0.5 mAh cm⁻². **(b)** Cycling stability of Li-H battery with alkaline electrolyte at a current density of 0.5 mA cm⁻² with a fixed capacity of 1.0 mAh cm⁻². **(c)** 3D volume calculation

model and radius (in Å) for H_3PO_4 and H_2O . **(d)** Snapshots of the AIMD simulation box of water and the typical binding structure between water molecules with corresponding color-filled IRI analysis diagram. **(e)** Snapshots of the AIMD simulation box of high concentration H_3PO_4 electrolyte (14.5 M) and the typical binding structures between H_2O and H_3PO_4 molecules with corresponding color-filled IRI analysis diagrams. The color bar is an IRI interaction bond strength standard card. **(f)** AIMD simulation result of the interface between water and LATP. **(g)** XRD comparison of different surfaces of LATP before and after cycling. SEM images of different surfaces of LATP contacting with **(h)** anode or **(i)** cathode proton-rich electrolyte after cycling.

In the high concentration H_3PO_4 electrolyte, because the larger molecular volume of H_3PO_4 molecules than H_2O molecules (Figure S15c), and also the stronger interaction between them as confirmed by the ab initio molecular dynamics (AIMD) simulations combining the interaction region indicator (IRI) analysis, H_2O molecules are bound by H_3PO_4 molecules, making them relatively difficult for protons (H^+) from the coordinated H_2O molecules or interrelated H_3PO_4 molecules to continuously attack the LATP (Figure S15d,e). Meanwhile, due to the presence of a large amount of PO_4 tetrahedron in the LATP structure and the high concentrated H_3PO_4 molecules in the proton-rich electrolyte, a locally high concentration region can be formed in the interface between LATP and the cathode electrolyte. In the interface, as shown in the AIMD simulation results (Figure 4h), H_3PO_4 molecules will coordinate with metal cation (M) on the surface of LATP to form M-O-P, or bind with M-O and P-O through hydrogen bonds (to form M-O \cdots H-P and P-O \cdots H-P). And the H_2O molecules in the proton rich electrolyte will be confined through strong hydrogen bonding with surface bonded H_3PO_4 molecules to prevent them from further attacking LATP. This also confirms the observation of LiH_2PO_4 (M-O-P) at the interface when the battery is deeply discharged in Figure 4a. While in the pure water environment (Figure S15f), H_2O molecules will continuously undergo the chemical reactions to form MO-H and M-OH or P-OH as well as its coordination with separated M, leading to the expansion of LATP cracks and the damage of its mechanical properties, ultimately leading to battery failure.

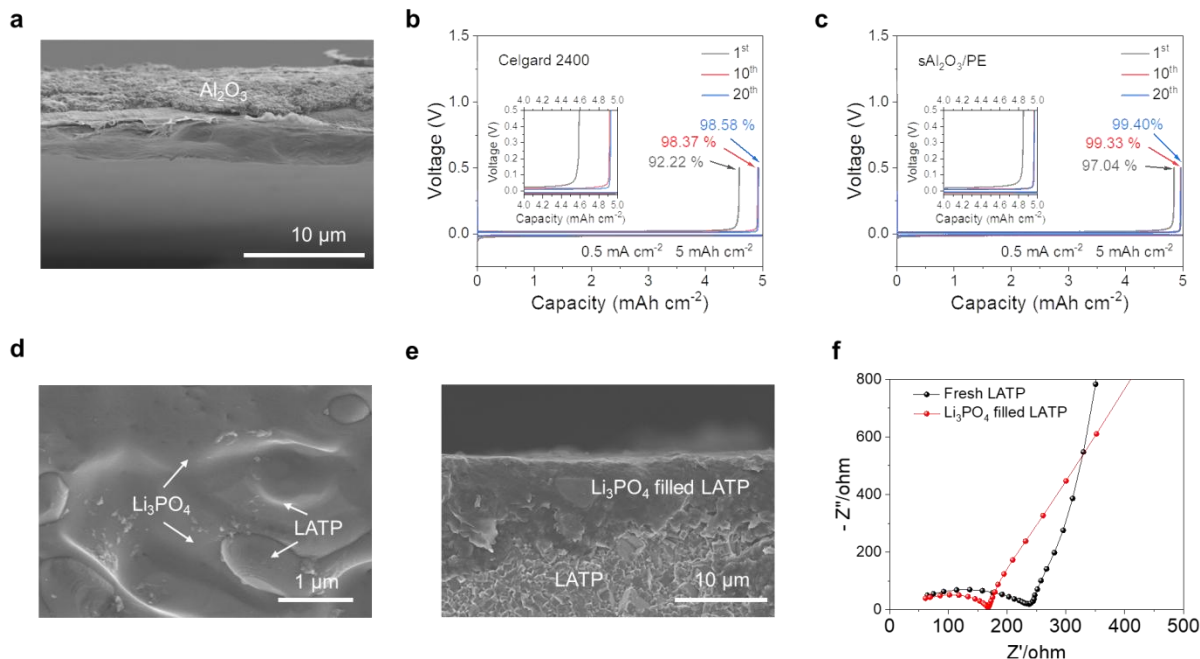


Figure S16. Strategies for improving the CE of anode-free Li-H battery. Strategy 1. Replacing typical PP film of Celgard 2400 with $s\text{Al}_2\text{O}_3/\text{PE}$ to improve the deposition/stripping efficiency of Li. (a) SEM of the cross section of $s\text{Al}_2\text{O}_3/\text{PE}$. The different cycles galvanostatic voltage profiles of the Li//Cu asymmetric batteries paired with (b) Celgard 2400 and (c) $s\text{Al}_2\text{O}_3/\text{PE}$. Strategy 2. Filling the grain boundaries of LATP using molten lithium phosphate (Li_3PO_4). SEM images of the (d) surface and (e) cross-section of LATP filled with Li_3PO_4 . (f) Impedance measurements of the anode-free Li-H batteries with or without Li_3PO_4 filling.

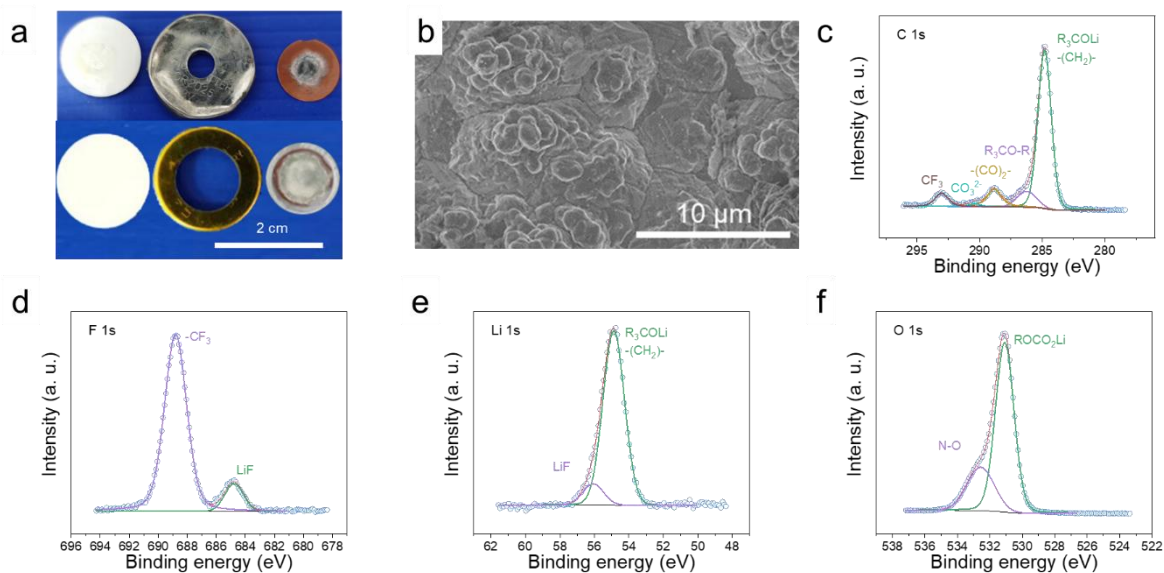


Figure S17. Characteristics of the SEI on the Cu surface of cycled anode-free Li-H cell. (a) Pictures of deposited lithium metal with different areas of 0.2 and 1.0 cm². **(b)** Surface morphology and the corresponding high resolution XPS spectra of carbon (C 1s) **(c)**, fluorine (F 1s) **(d)**, lithium (Li 1s) **(e)**, and oxygen (O 1s) **(f)**.

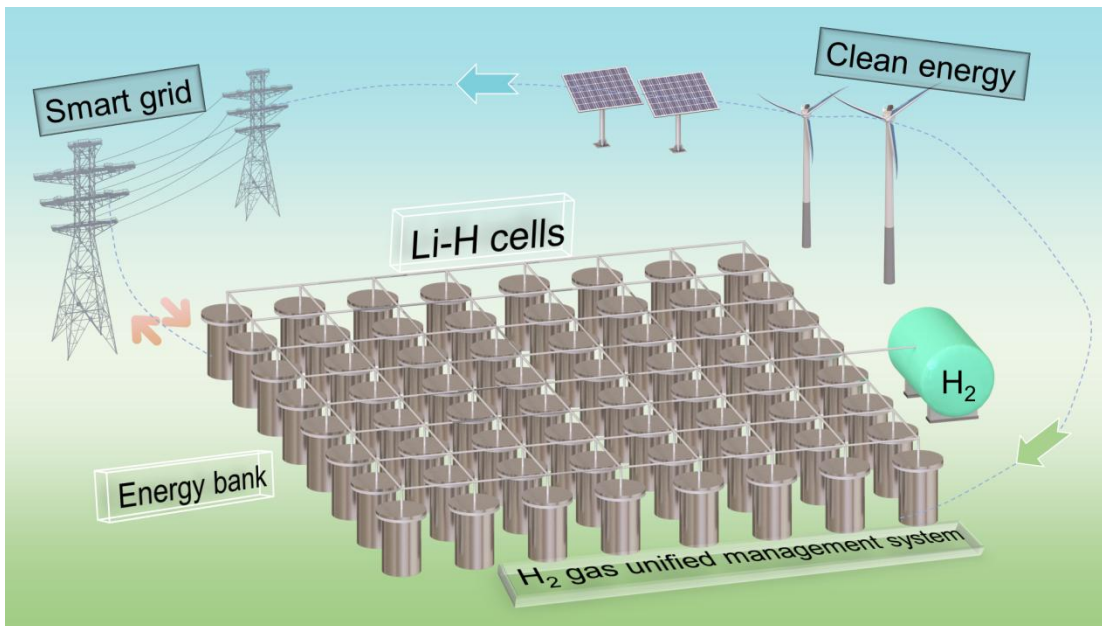


Figure S18. Future production of Li-H battery system with high utilization of H₂ gas. Schematic of H₂ gas unified management system for the Li-H battery.

Table S1. Theoretical specific energy of Li-H battery with different discharge products.

Discharge Products (1 e ⁻ transfer)	Theoretical Working Voltage (V)	Theoretical Specific Energy (Wh kg ⁻¹)
LiOH + 1/2 H ₂	2.63	2825
LiCl + 1/2 H ₂	3.04	1878
LiH ₂ PO ₄ + 1/2 H ₂	3.04	776
LiNO ₃ + 1/2 H ₂	3.04	1164
1/2 Li ₂ SO ₄ + 1/2 H ₂	>3.04	~1456
1/2 Li ₂ CO ₃ + 1/2 H ₂	2.85	2012
HCOOLi + 1/2 H ₂	2.93	1482
CH ₃ COOLi + 1/2 H ₂	2.90	1160
LiTFSI + 1/2 H ₂	3.04	283

Table S2. Parameters of Li-H battery with different concentrations of H₃PO₄ electrolytes.

Concentration (mol L ⁻¹)	Volume (μ L)	OCV (V)	Theoretical Capacity (mAh)	Capacity Available (mAh)	Utilization (%)
14.5	25	3.023	9.72	9.30	95.7
12	25	3.012	8.04	7.01	87.2
10	25	2.996	6.70	5.90	88.1

Table S3. The energy density evaluation of Li-H battery.

	H ₂	LiH ₂ PO ₄	LiOH	H ₃ PO ₄	Pt/C	Ru/C	Cu	Organic electrolyte	LATP	GDL	sAl ₂ O ₃ /PE	GF	Total
Ratio with utilization (%)	125	75	50	10	100	100	100	100	100	100	100	100	89
Weight (g)	0.0018 653	0.05815 8	0.008 934	0.0073 11	0.00 01	0.0 001	0.0 035 8	5.9*10 ⁻⁶	0.157 27	0.02 51	0.003	0.0 157	0.28 11
Capacity (mAh)													20
Voltage (V)													2.8
Energy density with storage tank (Wh/kg)													177

The detailed calculation of energy density considering utilizations based on our results is summarized as follows:

Part 1: For lithium salts (LiH₂PO₄), our highest utilization can reach 99.37%. And a mixed lithium (75% LiH₂PO₄ + 50% LiOH) supplementation solution was proposed to compensate for the fact that the CE in the anode-free Li-H battery currently is difficult to reach 100% to ensure its long-term cycling. Based on the provided lithium replenishment strategy, the lithium salt part is expected to further increase the energy density of the battery by 7.54 Wh kg⁻¹.

Part 2: Based on the results regarding the utilization of proton-rich electrolytes, it is necessary to reserve approximately 5% ~ 13% of the H₃PO₄ electrolyte to maintain the wetting of the cathode electrolyte interface. We take a median value of 10% for the cost and energy density calculations. Therefore, we have also added this part of the mass to the anode-free Li-H battery, which will reduce the energy density of the battery by 5.34 Wh kg⁻¹.

Part 3: For H₂ gas, the utilization of H₂ gas can reach ≥91.6%. We have demonstrated that providing excessive 25% or 13% H₂ gas can ensure stable operation of the battery. This part will reduce the energy density by 0.265 Wh kg⁻¹ if we provide excessive 25% H₂ gas. We believe this part will be able to receive optimization after the reasonable design of the cell structure in future.

Part 4: Modifications to enhance CE. The replacement of the sAl₂O₃/PE film and the Li₃PO₄ coating on the LATP surface will reduce the energy density by 2 Wh kg⁻¹.

Part 5: In addition to the above active materials, we further deducted the energy density from the weight ratio of the H₂ gas storage tank. Its weight is expected to be controlled in an acceptable proportion (within 11 %) after cell design engineering referring to the traditional Ni-H₂ battery (*J. Energy* **6**, 28-33 (1982).). This part is expected to be further improved by using low-pressure H₂ gas or a better battery gas management system.

Therefore, taking into account all the above 5 parts including key active materials, modifications, the gas storage tank and the excessive H₂ gas, we have finally obtained an energy density of 177 Wh kg⁻¹ = (199 + 7.54 - 5.34 - 0.265 - 2) × 0.89 at this stage. It is worth noting that the universality of H₂ gas cathode will enable the Li-H battery a greater room for theoretical energy density improvement in the future (≤ 2825 Wh kg⁻¹).

Table S4. Electrochemical performance of the Li-H battery compared with other gas electrode batteries with the ceramic separator.

	Cathode catalyst	Discharge product	Current density	Discharge/charge potential (V)	Overpotential (V)	RTE (%)	Maximum capacity	Cyclic stability	Operating temperature range	Ref.
Li-H ₂ battery	Pt/C	Li ⁺ / H ₂	0.025 mA cm ⁻² 1.0 mA cm ⁻²	2.9948 / 3.0027 2.82 /3.06	0.0079 0.24	99.70% 91.65%	25 mAh cm ⁻² / 22000 mAh g ⁻¹	1900 hours/ 480 cycles	Room temperature	This work
Li-air battery	TiC	Li ₂ O ₂	1 mA cm ⁻²	~ 2.5 / ~3.5	~ 1.0	71.00%	/	100 cycles	/	Nat. Mater. 2013, 12, 1050–1056.
Li-air battery	CNT	Li ₂ O ₂	500 mA g ⁻¹	~ 2.8 / ~ 4.1	1.3	68.30%	12020 mAh g ⁻¹	150 cycles	/	Nature 2021, 592, 551–557.
Li-air battery	carbon and Ni-nitrate composite cathodes	Li ₂ O	0.1 mA cm ⁻²	~ 2.76 / ~ 2.96	0.2	89.00%	11 mAh cm ⁻²	150 cycles	150 °C	Science 2018, 361, 777–781.
Li-CO ₂ battery	Single Fe atoms /3D N,S-codoped holey graphene	Li ₂ CO ₃ + C	100 mA g ⁻¹	2.78 /3.95	1.17	70.40%	23174 mAh g ⁻¹	210 cycles	/	Adv. Mater. 2020, 32, 1907436
Li-CO ₂ battery	MoS ₂ nanoflakes	Li ₂ CO ₃ +C	100 mA g ⁻¹	2.92 /4.27	~1.35	68%	/	500 cycles	/	Adv. Mater. 2019, 31, 1902518.
Li-CO ₂ battery	Bamboo-Like N-CNT	Li ₂ CO ₃ +C	50 mA g ⁻¹	2.72 /3.98	1.26	68.2%	23328 mAh g ⁻¹	800 hours	/	Adv. Mater. 2019, 31, 1903852.
Li-CO ₂ battery	Ru/carbon nanofiber	Li ₂ CO ₃ +C	100 mA g ⁻¹	2.80 /4.15	1.35	67.40%	/	50 cycles	/	Energ. Environ. Sci. 2019, 12, 1100- 1107.

References:

- [1] a, W. Chen, G. Li, A. Pei, Y. Li, L. Liao, H. Wang, J. Wan, Z. Liang, G. Chen, H. Zhang, J. Wang, Y. Cui, *Nat. Energy* **2018**, *3*, 428-435; b, Z. Zhu, M. Wang, Y. Meng, Z. Lin, Y. Cui, W. Chen, *Nano Letters* **2020**, *20*, 3278-3283; c, Z. Zhu, Y. Meng, Y. Cui, W. Chen, *Adv. Funct. Mater.* **2021**, *31*, 2101024; d, Z. Zhu, W. Wang, Y. Yin, Y. Meng, Z. Liu, T. Jiang, Q. Peng, J. Sun, W. Chen, *J Am Chem Soc* **2021**, *143*, 20302-20308.
- [2] J. D. Dunlop, J. F. Stockel, *J. Energy* **1982**, *6*, 28-33.
- [3] a, G. Kresse, J. Furthmüller, *Phys. Rev. B* **1996**, *54*, 11169; b, J. P. Perdew, K. Burke, M. Ernzerhof, *Phys. Rev. Lett.* **1996**, *77*, 3865; c, J. P. Perdew, Y. Wang, *Phys. Rev. B* **1992**, *45*, 13244.
- [4] G. Henkelman, B. P. Uberuaga, H. Jónsson, *J. Chem. Phys.* **2000**, *113*, 9901-9904.
- [5] V. Wang, N. Xu, J.-C. Liu, G. Tang, W.-T. Geng, *Comput. Phys. Commun.* **2021**, *267*, 108033.
- [6] a, T. Lu, Q. Chen, *Chem. Methods* **2021**, *1*, 231-239; b, T. Lu, F. Chen, *Journal of Computational Chemistry* **2012**, *33*, 580-592.